

Deep Learning for Radiation Dose Estimation

Masterarbeit

Eingereicht von:	Gutwein, Simon
Studiengang:	Medizinische Strahlenwissenschaften
Matrikelnummer:	5419474
Betreuer:	Prof. Dr. Daniela Thorwarth
Bearbeitungszeit:	von 16.09.2021 bis 16.03.2022

Eberhard Karls Universität Tübingen

Universitätsklinik für Radioonkologie // Sektion für Medizinische Physik

Hoppe-Seyler-Straße 6, 72076 Tübingen

Abstract

Hello, here is some text without a meaning. This text should show what a printed text will look like at this place. If you read this text, you will get no information. Really? Is there no information? Is there a difference between this text and some nonsense like “Huardest gefburn”? Kjift – not at all! A blind text like this gives you information about the selected font, how the letters are written and an impression of the look. This text should contain all letters of the alphabet and it should be written in of the original language. There is no need for special content, but the length of words should match the language.

Contents

Abbildungsverzeichnis	iii
Tabellenverzeichnis	iv
Abkürzungsverzeichnis	v
1 Introduction	1
2 Previous Work	5
3 Medical Knowledge	7
4 Material and Methods	8
4.1 Network Architecture	8
4.2 Dataloading	8
4.3 Network Input & Output	9
4.3.1 Network Input	9
4.3.2 Network Output	11
4.4 Training Data Generation	11
4.5 Evaluation Metrics	12
4.6 Hypotheses and Experiments	12
4.6.1 General Applicability	12
4.6.2 Poor Initial Translatability	13
4.6.3 Increased Robustness	14
4.6.4 Underlying Physics	14
4.7 Patient Data	14
5 Results	16
5.1 These 1 / Experiment 1	16
5.2 These 2 / Experiment 2	16
5.3 These 3 / Experiment 3	18
5.4 These 4 / Experiment 4	19
6 Discussion	20
7 Acknowledgement	21
Appendix	28

List of Figures

Figure 1:	Basic scheme of adapted network architecture with a downsampling ratio of 8 and a maximum depth of 512 in the bottleneck layer. Input dimensions: $5 \times W \times H \times D$; Output dimensions: $1 \times W \times H \times D$. . .	8
Figure 2:	Dataloading scheme for memory efficient patch based dataloading for 3D training volumes. A subset of patches from one training volume is depicted in one color shade.	9
Figure 3:	Exemplary input and output for a single segment of a prostate plan. (a): beam shape, (b): center beam line distance, (c): source distance, (d): CT, (e): radiological depth, (f): dose distribution,	11
Figure 4:	Gamma test for two points r_{passed} and r_{failed} and the reference point r_m for a 2D (X,Y) space case. Orange and brown rings indicate distance and dose parameter acceptance margins respectively. The Gray sphere represents the set of all points that pass the gamma test. Green and Red arrow indicate a passed and failed gamma test for the given reference point r_m , dose and spatial parameter.	13
Figure 5:	dvh for prostate cancer test plan with gamma passrate of 99.36%.	17
Figure 6:	Dose prediction example on isocentric slice on prostate cancer patient from test cohort with prostate data only trained model. From left to right: target dose; dose prediction; gamma map for isocentric slice with a gamma pass rate of 98.02%	18
Figure 7:	Dose prediction example on isocentric slice on breast cancer patient from test cohort with prostate data only trained model. From left to right: target dose; dose prediction; gamma map for isocentric slice with a gamma pass rate of 53.78%	18
Figure 8:	Prediction accuracy comparison between prostate only and mixed trained models. Passrates for liver, mamma and H&N are combined into one group of ‘mixed’ data. Significance level using a wilcoxon signed-ranked test are shown above the compared dataseries. zusätzlich plot für einzelne entities also leber, mamma, h&N einzeln, sternchen erklären oder direkt obendrüber schreiben, feste convention finden wie ich die beiden Model nennen will	29
Figure 9:	Prediction accuracy for all segments of the test data.	30
Figure 10:	Prediction accuracy of each segment with respect to field size for prostate only and mixed trained model.	31
Figure 11:	Coronal, sagital and transversal view of the dose distributions for 100, 200 and 300 px depth in the phantom volume	32

List of Tables

Table 1:	Patient data information for Prostate-Only as well as Mixed-Entity trained model and testing data set. Fieldsizes are given as mean (standard deviation).	15
Table 2:	Summary of gamma passrates for liver, mamma, head and lymphnodes tumor patients, hier noch min max einfügen	17
Table 3:	Summary of gamma passrates for liver, mamma, head and lymphnodes tumor patients min max hinzufügen	19
Table 4:	Gamma passrates for prostate only and mixed trained models for different water slab phantom positions inside an air volume. Water slab thickness was 200 pixels.	19

Abkürzungsverzeichnis

H&N	head & neck	14
GPU	graphics processing unit	8
RAM	random-access memory	8
FF	flattening filter	10
ERE	electron return effect	11
HPC	high-performance computing	11
MLC	multi leaf collimator	12
SSD	source surface distance	13

1 Introduction

Introduction

- **Genereller Ablauf am MR-Linac stand jetzt**
- Person kommt, bekommt ein CT für initiale Planung, danach wird dann bei Bestrahlung des Patienten ein MRT von dem Patienten gemacht. Registrierung von CT und MRT und adaption von contours auf MRT. Dann Online-Plan adaption bei dem Plan aufgrund von adapt to position oder shape. Results in no adaption or adaption of segments shape, monitor units or both. This is repeated for each treatment fraction of the patient (Adaptive radiotherapy: The Elekta Unity MR-linac concept). Eingehen auf Limitationen, intrafraction movement, (paper suchen), adaptation
- **Wie soll der Ablauf einmal aussehen beim MR-Linac**
- Goal is to achieve a MRi-only treatment workflow, including imaging with MRI contouring on MRI and planning and calculation of plans on mri. dose calculation is not possible on mri data because mri is not a quantitative imaging modality, meaning pixel values give no information about the electron density of the underlying tissue or body part. therefore synthetic ct images need to be created from mri images, which enable dose calculations.
- **Und dann auf Dosisdeposition eingehen / Was ist aktuelle Methode** hier noch viel verschieben nach material und methodik
- (<http://dx.doi.org/10.1118/1.2795842>) monte carlo simulations are currently used for dose calculation for radiotreatment plans in a clinical setting. The interactions of photons in human tissue in the energy spectrum of interest for external beam therapy transfer the photon energy on to electrons or positrons. these particles then transfer their energy into the surrounding tissue. before energy deposition the photon and especially the electron undergo a number of elastic and non elastic interactions with atoms. In the process the main energy loss is caused by inelastic collisions and radiative interactions. the collisions result in ionization and therefore secondary electrons. radative interactions result in a energy trasnfer back to photons. the sum of these phenomena in a photon field results in a coupled electron-photon shower, which can be described by a coupled set of integrodifferential transport equations. due to the lack of a analytical solution, without any

major simplifications and assumptions for conditions, the monte carlo algorithm is used to simulate a multitude of particle histories in the desired target volume. particle histories describe the exact way of a photon from the source to its point in the volume where it has lost all of its energy including energy transport to secondary electrons in the process of collisions. the stochastic nature of the interaction processes of photons and electrons need for a large number of simulated particles to achieve an accurate result of dose deposition. the entirety of all simulated particles then results in an accurate dose distribution which can be used for treatment planning. the need for particle histories in the magnitude of 10^7 to 10^{11} for accurate dose estimations, result in long simulation times.

- Wo findet Deep Learning Anwendung (Bezug zu Medizin)
- Deep learning and especially computer vision is already present in current research of Biology, Physics as well as medicine. there are a multiple fields in which CV can be applied to fields such as dermatology (<https://sci-hub.ru/10.1038/nature21056>), radiology (<https://sci-hub.ru/10.1038/srep24454>, <https://sci-hub.ru/10.1097/rli.0000000000000000>), cardiology (<https://arxiv.org/abs/1708.09843>) or pathology (<https://www.nature.com/articles/020-58467-9.pdf>)
- Einleitung zu Deep Learning
- . deep learning is a preferred tool due to its short inference times as well as super human performance level on certain tasks. the implementation of the fully convolutional network (<https://arxiv.org/pdf/1411.4038.pdf>) and its further development of the U-Net utilizing data from higher level representations of the data in the form of skip connections (<https://arxiv.org/abs/1505.04597>) have revolutionized the application of deep learning for image data and 3d data in the form of a 3D-UNets.
- Was ist die Contribution / Aims <- Ziel: Dosisvorhersage mit DL, möglichst robust
- In this paper we investigate the capabilities of deep learning in the field of dose predictions for radio treatment plans. we aimed to achieve a robust dose prediction irrespective of the body region of interest and irrespective of the complexity of the treatment plan.
-

Show why Radiotherapy is so important: search for sources of application of radiotherapy for different entities. Prostate: [1–3] Mamma: [4–6] Head & Neck: [7–10] Liver: [11–15] Lymph Nodes: [16–20]

Was ich noch brauche: Infos über MR-Linac, was ist die Vision hinter dem MR Linac (online adaption)

The use of Magnet Resonance Imaging (MRI) during radiotherapy has opened a variety of new opportunities for treatment optimization. MRI provides a better contrast in soft tissue areas of the body, compared to conventional computed tomography (CT), and can be used to assess functional image data from the patient in real time. The enhanced contrast leads to better organs at risk (OAR) and tumor volume delineation. (doi:10.1016/S0360-3016(03)01446-9). Recent research efforts are exploring the capabilities of the hybrid MRI linear accelerator (MRI-Linac) (doi:10.1007/s00066-018-1386-z, doi:10.1016/j.radonc.2007.10.034, doi:10.1002/acm2.12233). The introduction of the MRI-Linac has transformed the clinical workflow for radiotherapy as well as treatment planning. Patients are required to receive one CT for initial treatment planning. For radiation in each fraction, the initial plan is registered on the current MRI and optionally adapted to shift or size variation of the tumor volume (doi:10.1016/j.ctro.2019.04.001). Goal is to reach an MRI-only-workflow where image acquisition, treatment planning and radiotherapy only involve the MRI-Linac. To achieve this goal multiple steps in the clinical workflow need to be adapted

behind MRI Linac is an radiotreatment adaption in an online manner, meaning that a shift of the tumor volume and changes to the patients anatomy due to movement can be considered to adapt the treatmentplan. This results in smaller safety margins (doi:10.1102/1470-7330.2004.0054) for tumor volumes and ultimately result in a lower delivered dose to organs at risk. To achieve this ultimate goal, multiple steps, such as anatomy segmentation, treatmentplan adaption and dose deposition simulations need to be able to be performed in real-time.

Welche besonderheiten gibt es bei einem MR-Linac im Vergleich zu einem normalem Bestraher (Stichworte: ERE, Electron Deposition Shift) Wie funktioniert normale Dosisberechnung (Monte Carlo doi:10.1118/1.598917), warum ist der Nutzen davon limitiert wenn man in die online Adaption möchte.

However, since MC simulation is a stochastic process, the resulting dose map contains inherent quantum noise whose variance is inversely proportional to the number of the simulation histories and, accordingly, to the simulation time. Typically, achieving clinically acceptable precision requires hours of CPU computation time. Graphics processing unit (GPU)-based parallel computation frameworks can accelerate MC simulation to a few minutes for a typical IMRT/VMAT plan (doi:10.1088/0031-9155/55/11/006)

However, several areas in the clinical workflow require real-time dose calculation, such as

inverse optimization of the treatment planning process for IMRT and VMAT (doi:10.1088/2632-2153/abdbfe) especially online radiotherapy and online plan adaption are limited by the time needed to recalculate dose distributions of beam settings and patient anatomies due to moving organs (doi:10.1016/j.clon.2018.08.001)

Machine Learning Teil: Wie wird Machine Learning in verschiedenen bereichen der bestrahlungsplanung bezüglich MRI genutzt: Eine Implementierung und Nutzung dieser könnte zum Erreichen einer Online-Bestrahlungsadaption führen

1. Autosegmentation ([21, 22]) aswell as uncertainty ([23])
2. Radio Treatment Plan optimization ([24, 25])
3. Dose Estimation ([26, 27] active denoising of lower history MC Simulations (doi:10.1002/mp.13856))
4. Pseudo CT ([28–30])

2 Previous Work

Previous Work (evtl. mit in die Introduction) / Related Work

- Bezug nehmen auf
- DeepDose
- Weitere Paper zu dem Thema (Protonen mit LSTM, weitere Dosisberechnungen, siehe Paper, dass Christian gesendet hat)

Radiotherapy:

<https://iopscience.iop.org/article/10.1088/1361-6560/ab7630>

using 3d unet architecture and patch based approach to estimate dose in prostate cancer patients for individual segments of an entire treatmentplan. input data fro unet include patient information in the form of ct, as well as information form the accellerator such as beam angle and beam shape. they achieve very good results with 99.9 ± 0.3 for 3%/3mm gamma passrate. and 1 minute for dose estimation for one patient in total

<https://aapm.onlinelibrary.wiley.com/doi/full/10.1002/mp.14658>

dose prediction for protonfields in highly heterogenous tissues using long short term memory (LSTM) networks. it treats the affected part of the tissue as a sequence of 2 inputs and calculates the respective dose in the scheme of a marching beam trough the tissue. the reach robustnes by generating artificial phantom cases for the dose predictions. results show 98.57% gamma passrate (1%/3mm) for artificial cases and an average gama passrate of 97.85% for patient test cases.

<https://www.ncbi.nlm.nih.gov/pmc/articles/PMC7870566/>

dose estimation for segments was achieved by combining fluence maps from segments aswell as patient anatomies. they generated 3d fluence volumes from 2d fluence maps including information of beam angle. an 3d unet like architecture with residual blocks inside the convolutional building block was used for prediction. the overall dose variation normalized to the prescribed dose was $0.17\% \pm 2.28\%$.

High-Particle Simulation of Monte-Carlo Dose Distribution with 3D ConvLSTMs

to achieve a precise dose distribution in the desired 3d volume they use an approach utilizing active denoising of monte carlo simulations with deep learning. they implemented a 3d LSTM architecture inside the skipconnection of a 3d unet architecture. a sequence of noisy monte carlo simulations was used as the input and the output is the denoised

doe prediction. the loss function was constructed from the L1 loss and the structural similarity index measure. gamma pass rate for 5 patients was $94.1\% \pm 1.2\%$ and the L1 was $4 \cdot 10^{-3} \pm 1 \cdot 10^{-3}$.

DeepMCDose: A Deep Learning Method for Efficient Monte Carlo Beamlet Dose Calculation by Predictive Denoising in MR-Guided Radiotherapy the proposed network consists of 3 seperate Unets to seperately analyse the 3 input channels consisting of unsampled MC dose, MC x-ray fluence and the ct geometry for a single beamlet. the output from each network is then combined to calculate the residual needed dose to achieve the denoised dose distribution. the normalized mean absolute error reduced from 25.7% on the undersampllet MC simulation to 0.106% for the network output. The simulation of 380s for an fully sampled beamlet was reduced to 220 ms for the network prediction

<https://www.ncbi.nlm.nih.gov/pmc/articles/PMC7115345/>

3 Medical Knowledge

Medical Base Knowledge:

wieso schreibe ich hier über radiotherapy - wie wird sie angewendet - was ist konverntionell
- linear beschleuniger, ablauf für patienten - planung dosis nebenwirkungen eingehen - auf
was zielt der MR linac ab überleitung zu dosisberechnungs algorithmen - monte carlo - in
detail EGSnrc eingehen und erläutern was der vorteil hier für uns ist (einzelne segmente,
erläuterung, dass ein plan aus verschiedenen segmenten besteht die aufsummiert werden)
kurz über wechselwirkungen reden und wie die dosisdeposition mit monte carlo simuliert
wird. dann kurz erläutern warum ich das hier eigentlich grade beschreibe - darauf eingehen
dass trainingsdaten halt mit diesem egsrc simuliert werden

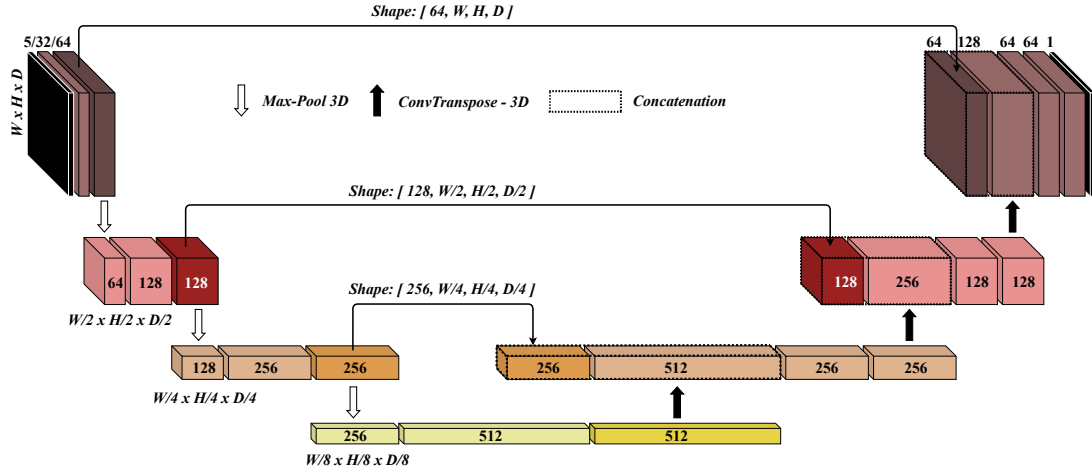


Figure 1: Basic scheme of adapted network architecture with a downsampling ratio of 8 and a maximum depth of 512 in the bottleneck layer. Input dimensions: $5 \times W \times H \times D$; Output dimensions: $1 \times W \times H \times D$

4 Material and Methods

4.1 Network Architecture

The network architecture (fig. 1) is based on a basic 3D-UNet implemented by Ronneberger et al. [31] with slight adaptations in downsampling depth, due to memory limitations when using 3D data. We used a downsampling ratio of 8 and a maximum layer depth of 512 in the bottleneck connection. Skip connections are used after each convolutional steps before each pooling layer. To include a multitude of information from the patient as well as the accelerator, we used five input volumes concatenated along the forth dimension, resulting in an input volume of size $5 \times width (W) \times height (H) \times depth (D)$. As the base resolution for all volumes we used the resolution of our CT scans with voxel dimensions of $1.1718 \times 1.1718 \times 3mm^3$ in the coronal, sagittal, and tanversal plane.

4.2 Dataloading

Memory usage is a serious concern in the application of deep learning and espeacially when dealing with 3D data sets. In our case not only the memory usage in the graphics processing unit (GPU) but in the random-access memory (RAM) is of importance. For each training epoch, the network sees all present training data. In most applications all data can be loaded into the RAM and is then passed onto the GPU. A solution to this problem is to load data on the fly into the RAM and then process it. This is not applicable because of the immense size of the 3D volumes (multiple 100 MB per volume) that are

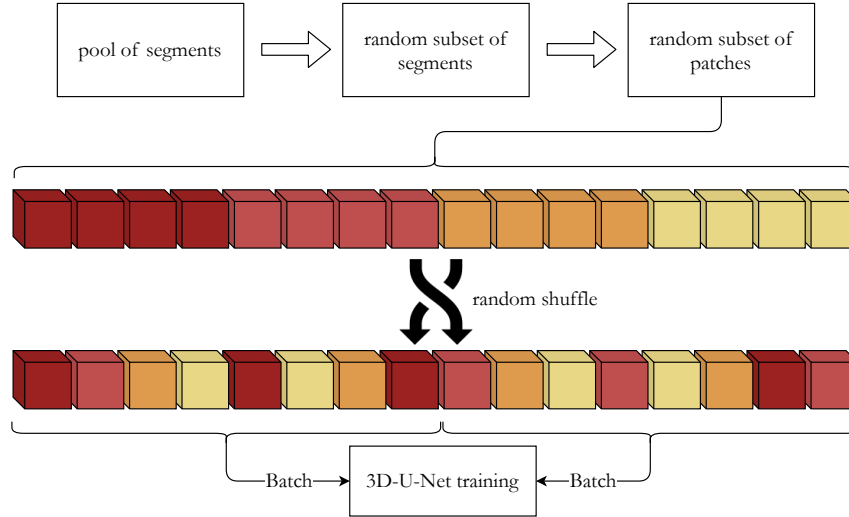


Figure 2: Dataloading scheme for memory efficient patch based dataloading for 3D training volumes. A subset of patches from one training volume is depicted in one color shade.

used for training. We therefore developed an partial on the fly dataloading inspired by the *Queue* class from Pérez-García et al. [32]. Due to the quantitative nature of our input data, we were not able to use data augmentation for our input data. To still achieve some additional variation in training data we used the approach of patch based training. A multitude of patches can therefore be extracted from the same volume, increasing the variety in training data while using the relatively small number of training volumes. To combine the semi-on-the-fly dataloading and the patch based training, multiple volumes are loaded into the RAM and then processed together. fig. 2 shows a scheme of this dataloading approach. A fixed amount of training data is loaded from the randomized training data pool and loaded into the RAM. From this set of training volumes a subset of patches is extracted from each volume and stored in a queue of patches, which is then shuffled and batch wise passed onto the GPU and the network.

4.3 Network Input & Output

4.3.1 Network Input

The network expects five 3D volumes concatenated along their fourth dimension as input. These five 3D volumes (fig. 3) combine different spatial, anatomical aswell as accelerator information into the training data. By doing so gantry aswell as accelerator head information can be directly translated into 3D space, which makes them interpretable for the network.

- (a) **Beam Shape:** The trajectory of the beamshape into 3D space if of crucial importance. It is most important accelerator information for the network. It combines leaf configurations as well as gantry angle into one volume. It acts in some way as a binary indexing mask giving the network information about which voxel is intersected by the beams trajectory into 3D space. To additionally account for the outputfactor the fieldsize of that specific segment is stored in each voxel intersected by the beam field. The output factor describes the physical process of increasing photon in-scatter into the central beamline for increasing fieldsizes.

- (b) **Center Beam Line Distance:** The beam of a linear accelerator is best defined in the central beam line. The use of flattening filter (FF) mostly corrects for this occurence. The distance from the central beam line is therefore of importance for the dose deposition. The minimum distance of each voxel from the central beam line accounting voxel dimensionality is saved in this mask. -> hier mal nochmal drüber reden

- (c) **Source Distance:** The radiation pattern of photons from the accelerator head can be assumed to be the front of a spherical wave. The photon fluence is therefore decreasing with the square of the distance from the source. The source distance mask takes this physical relationship into account. Each voxel within the volume is assigned its distance to the source, taking into account the different voxel dimensions in the different spatial directions.

- (d) **CT:** Dose deposition and particle interaction in genereal are defined by their energy aswell as the electron density of the affected volume. As the energy of the radiated photons is assumed constant, the impact of the electron density of the volume (in this case the patients anatomy) is mainly responsible to the different interaction processes of the photon and secondary electrons. The masks consists of the hounsfield units from the initial CT scan of the patient. Particles radiation from gantry angles below the treatment couch, interact partly inside the treatment couch, therefore it is included in the CT mask.

- (e) **Radiological Depth:** A photon or electron that passes trough the interaction medium loses its energy on its path. Therefore, the path that a particle follows through a medium is of highly relevant for the dose deposition effects that take place. The radi-

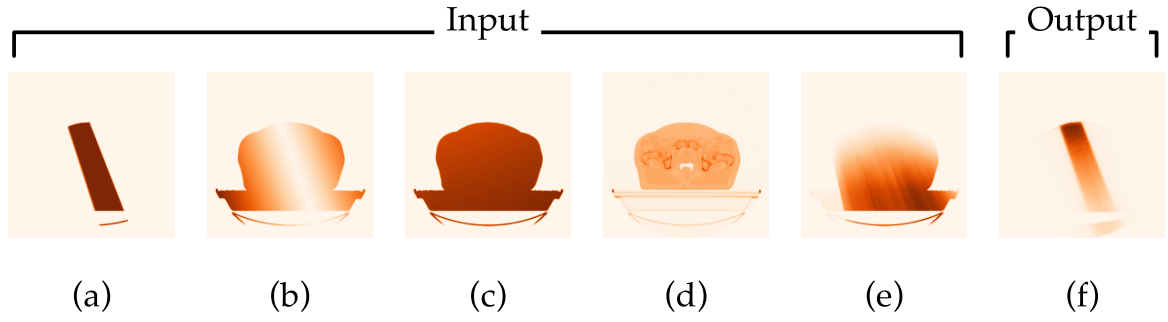


Figure 3: Exemplary input and output for a single segment of a prostate plan. (a): beam shape, (b): center beam line distance, (c): source distance, (d): CT, (e): radiological depth, (f): dose distribution,

ological depth combines the distance from the source as well as the interaction medium's density. It is the sum of the path length through a medium multiplied by the density of intersected voxels. Therefore the same spatial depth in a dense material results in a higher radiological depth than the same depth in soft tissue.

Particles interact negligibly in air, therefore were all masks set to zero where the CT mask was 150 HU over the HU for air. Air or low density volumes inside the body of the patient were not affected by this step, to account for the electron return effect (ERE) on the surface of air cavities inside the patient.

4.3.2 Network Output

The network combines the information from the five 3D volumes and yields a single volume with the respective dose distribution for the given input. Spatial dimensions for width, height, and depth as well as voxel dimensions are preserved during inference. In fig. 3 (f) an exemplary dose distribution for the respective inputs (a) - (e) is given.

4.4 Training Data Generation

All training data was generated from patient data taken from the institutional database of radiotherapy treatment plans. Information for all input masks are given in the CT scan, the dose file as well as the plan file. The patient's anatomy for the CT masks is taken from the CT files and adjusted to the right slice thickness, due to different acquisition protocols using 2 mm or 3 mm slice spacing. Dose distribution used as training target for each segment were calculated using the EGSnrc open source software package provided under [33]. The work of Friedel et al. enabled us to accurately simulate single segment dose distributions for the MR-Linac. Simulation of all segments was done using a remote high-

performance computing (HPC) solution provided by the state of Baden-Württemberg. Coordinate system orientation of the patients anatomy as well as multi leaf collimator (MLC) and gantry positions are given in the dose and plan file. Simulation of 10^7 particles took around 4 hours on average. The 3D input volumes to the network were calculated using in-house developed python scripts with the provided information from CT, dose and plan files. (GITHUB LINK?, hier noch näher drauf eingehen?)

4.5 Evaluation Metrics

Dose conformity of dose distributions are clinically assessed using the gamma-index metric first introduced by Low et al. [35] in 1998. The evaluation metric composed of two parametric values that set the criteria for which dose distributions are analysed. Spatial deviations aswell as deviations of dose are respected when analysing. Dose conformity is assessed by analyzing each individual voxel of a given dose distribution using the following equation:

$$\Gamma(r_m, r_c) = \sqrt{\frac{r^2(r_m, r_c)}{\Delta d_M^2} + \frac{\delta^2(r_m, r_c)}{\Delta D_M^2}} \quad (1)$$

where ΔD_M and Δd_M are the dose difference and spatial criterion respectively, in our case 3% and 3 mm. $r^2(r_m, r_c)$ and $\delta^2(r_m, r_c)$ are the squared spatial distance and dose difference from the reference point r_m to evaluation point r_c respetively. If $\Gamma \leq 1$ the criterion are passed. By evaluating the entire volume in that manner an overrall gamma passrate can be calulated with the following formula.

$$\gamma = \frac{NoT(\Gamma \leq 1)}{NoT} \quad (2)$$

where NoT is the number of points to be tested, in this case the number of voxels in the entire volume and $NoT(\Gamma \leq 1)$ is the number of tests that passed the gamma criterion following eq. 1. The equations eq. 1 and eq. 2 hold true for single aswell as multiple dimensions. A 2D example for a passed aswell as a failed gamma test is given in fig. 4.

4.6 Hypotheses and Experiments

4.6.1 General Applicability

Hypothesis

The network is able to learn the general dose deposition process from the given input taken from a multitude of radio treatment segments of one tumor entity. Dose

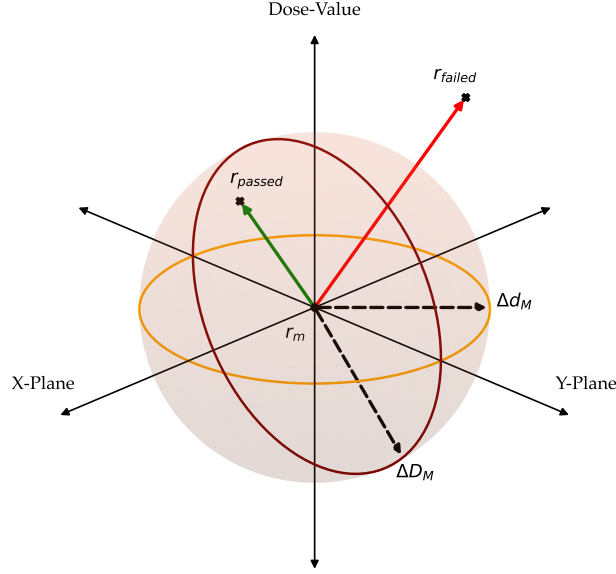


Figure 4: Gamma test for two points r_{passed} and r_{failed} and the reference point r_m for a 2D (X,Y) space case. Orange and brown rings indicate distance and dose parameter acceptance margins respectively. The Gray sphere represents the set of all points that pass the gamma test. Green and Red arrow indicate a passed and failed gamma test for the given reference point r_m , dose and spatial parameter.

predictions for segments of the same entity are accurate and robust.

Experiment

Training of the proposed 3D-UNet on a multitude of prostate cancer patient radio treatment segments. Dose conformaty assessment with the gamma passrate for each individual test segment aswell as entire test plans.

4.6.2 Poor Initial Translatability

Hypothesis

Different tumor sites vary drastically in segment shape, orientation and source surface distance (SSD). The SSD is, compared to other entities such as H&N, mostly constant for prostate cancer patients. The same holds true for tissue homogeneity aspects of the respective body regions, when comparing lower abdomen to e.g. H&N. We therefore assume that the network will not reach the previously achieved gamma passrates when testing on different tumor sites and patient anatomies.

Experiment

The from 4.6.1 *General Applicability* trained network is then used for inference on additional testing data from a multitude of tumor entities aswell as patient anatomies to test its translational capabilities to a varying set of input characteristics.

4.6.3 Increased Robustness

Hypothesis

The inclusion of a broader variety of segments shapes, sizes and positions inside the patients anatomy, as well as differing body regions and therefore varying SSD values and tissue densities result in a better robustness of the networks prediction accuracy.

Experiment

Network architecture aswell as training algorithm of the in *4.6.1 General Applicability* trained network are kept, while including additional trainign data from liver, breast and H&N patients. We therefore include liver, breast and head & neck (H&N) into the training of the same network from *Hypothesis 1*. The translational capabilities are then assed by testing the newly trained network on prostate, liver, breast, H&N and lymph node data. By doing this we asses if the network performance decreases on prostate data by including new tumor sites into the training data and we assess its performance on seen (prostate, liver, heaad & neck, breast) aswell as unseen treatment plan data (lymph nodes).

Experiment:

4.6.4 Underlying Physics

Hypothesis 4: The network is capable of learning the underlying physics of the dose depositiopn process.

Experiment 4: in order to decouple the dose delivery from the patient anatomy, we have created a phantom data set. The phantoms consist of an air volume in the shape of a cube with the dimensions $600 \times 600 \times 600 \text{ mm}^3$ ($512 \times 512 \times 200$ voxel for coronal, sagital and transversal plane, respectively). Within this air volume, a water slab is placed at various locations to account for the influence of the distance-squared law. in this volume, we now simulate and predict a 10×10 beam from 0° and observe the depth dose profile, as well as the coronal and sagital transverse dose profiles in the middle of the water volume. A multitude of aspects of the physics can distance-squared law, penumbra, qualitative and quantitative depth dose profiles, field divergence in central beamline.

4.7 Patient Data

All patients gave their informed written consent to this study, which was approved by the local ethical committee (ethics approval No. 659/2017BO1). patient data from our

Prostate-Only		Mixed-Entity				Testing
		Liver	Mamma	Head & Neck	Prostate	Lymphnodes
Number of Patients	45	15	15	15	15	15
Number of Segments	2342	819	656	929	720	659
Training / Validation / Testing	36/4/5	8/2/5	8/2/5	8/2/5	8/2/5	Only Testing
Fieldsize Training/Validation	36.5 (17.9)	24.1 (18.4)	40.7 (28.5)	63.0 (50.5)	35.5 (18.0)	N/A
Fieldsize Testing	34.5 (15.8)	22.8 (14.4)	40.6 (38.0)	68.9 (53.6)	34.6 (15.9)	26.0 (25.6)

Table 1: Patient data information for Prostate-Only as well as Mixed-Entity trained model and testing data set. Fieldsizes are given as mean (standard deviation).

institution previously treated at the mr linac. all plans were created by a medical physicist in agreement with a oncologist Welche Entitäten: Prostate only training: 45 prostate treatment plans with a total of 2342 Segments, 36/4/5 split für train / val / test split. with a mean fieldsize of $36.57 \pm 17.9 \text{ cm}^2$ for training / validation set and $34.57 \pm 15.86 \text{ cm}^2$ for the test set. mixed model 15 prostate with 720 segments, 35.49 ± 18.01 and 34.57 ± 15.86 15 liver 819 Segments 24.09 ± 18.36 and 22.81 ± 14.47 15 mamma 656 Segments 40.72 ± 28.48 and 40.60 ± 37.98 14 head & neck 929 segments in einem 8/2/5 split also in 32/8/20 train / validation / test ratio. aswell as 15 patient plans 659 segments for lymphnodes exclusively for testing with a mean fieldsize of 25.95 ± 25.59 as you can see in tab. 1 All patients gave their informed written consent to this study, which was approved by the local ethical committee (ethics approval No. 659/2017BO1).

5 Results

In the following section the experiments from each thesis to be tested are presented in a chronological manner.

5.1 These 1 / Experiment 1

das hier verschieben in methodik und dann inofs über wie lange es gedauert hat. The training of the network took around 11 days with a batchsize of 128 and $6.7 \cdot 10^5$ patches of size $32 \times 32 \times 32$ voxels. The training was performed on 4 nvidia gtx 2080 ti and a initial learning rate of 10^{-4} decreasing by a factor of 10 as soon as the validation loss or the gamma pass rate on the validation set did not decrease for 50 epochs. The training was stopped when no improvement was observed at a learning rate of 10^{-6} for 50 epochs. The model is able to predict the dose distributions for single segments. dose predictions for entire plans are achieved by a weighted summation according to the respective segment weight given by the provided patient plan.

The model reaches a mean gamma score of $96.16\% \pm 6.12\%$ (median: 98.02%) HIER NOCH MIN MAX, on the test dataset for prostate patients. (fig. 6) shows a qualitative example of a target dose and the respective dose prediction and gamma map for a prostate cancer patient in the isocentric slice. Qualitative analysis shows that the model is able to the correctly predict the beamshape for single segments. Penumbra as well as beamwidening are mapped correctly. fig. 5 shows a dose volume histogramm (DVH) for a test case of the prostate plan cohort. A very good dose agreement for high as well as low dose regions is reached. Slight deviations in smaller structures such as rectum and seminal vesicles can be observed, most likely due to the larger contribution of single voxel to the entire volume. auswertung von segmenten von prostate only für dieses Netzwerk. Hier noch bei DVH die femur heads rein bringen um zu schauen wie die dosis prediction bei unterschiedlichen densities ist. darauf eingehen in discussion.

5.2 These 2 / Experiment 2

The model shows rather poor translatability to other body regions. A summary over the prediction accuracy of the prostate only trained model for the tumor entities liver, mamma, H&N and lmyphnodes is given in tab. 2 gives a summary over. The model shows particular problems with breast cancer plans with a mean gamma passrate of $63.25 \pm 6.72\%$. An exemplary case is given by fig. 7 showing low accuracy in the high dose aswell as lower dose areas of the volume. eingehen auf die werte kurz erklären

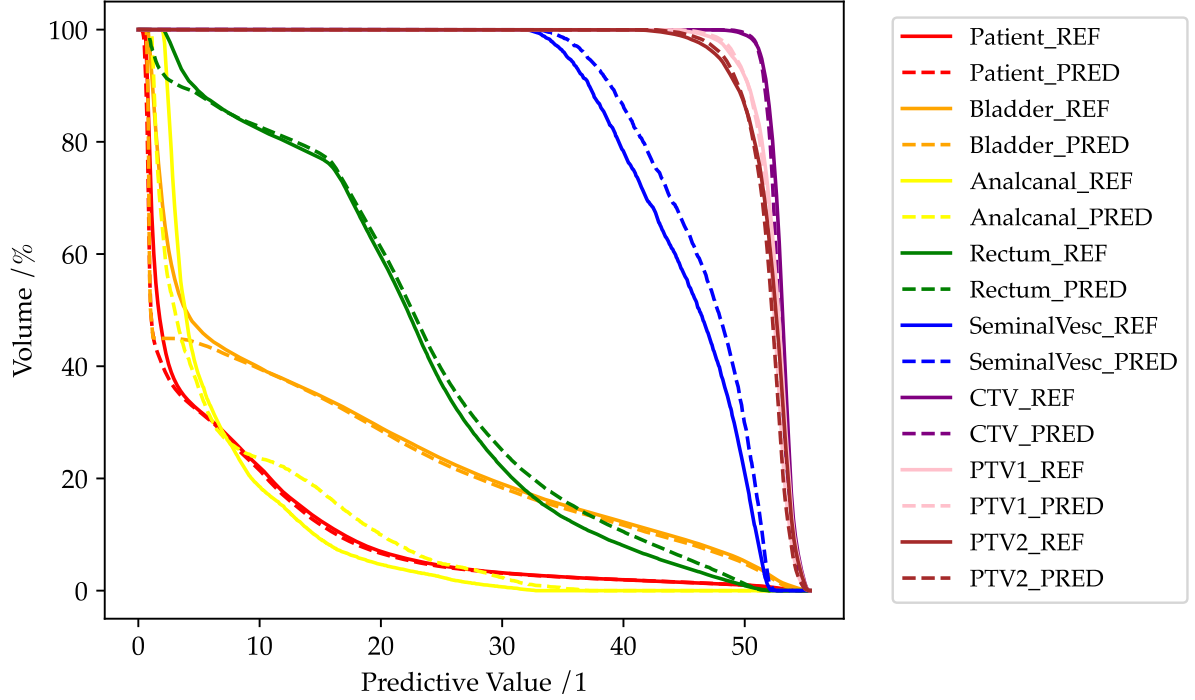


Figure 5: dvh for prostate cancer test plan with gamma passrate of 99.36.

	Liver	Mamma	H&N	LK
Number of Patient Plans /1	5	5	5	15
Mean Gamma Passrate	77.69	63.25	76.19	82.12
STD Gamma Passrate /%	10.13	6.72	4.99	11.51
Median Gamma Passrate	80.39	63.48	77.67	85.9

Table 2: Summary of gamma passrates for liver, mamma, head and lymphnodes tumor patients, hier noch min max einfügen



Figure 6: Dose prediction example on isocentric slice on prostate cancer patient from test cohort with prostate data only trained model. From left to right: target dose; dose prediction; gamma map for isocentric slice with a gamma pass rate of 98.02%



Figure 7: Dose prediction example on isocentric slice on breast cancer patient from test cohort with prostate data only trained model. From left to right: target dose; dose prediction; gamma map for isocentric slice with a gamma pass rate of 53.78%

5.3 These 3 / Experiment 3

The training of the network took around 9 days with a batchsize of 128 and $5.0 \cdot 10^5$ patches of size $32 \times 32 \times 32$ voxels. The training was performed on 4 nvidia gtx 2080 ti and a initial learning rate of 10^{-4} decreasing by a factor 10 as soon as the validation loss or the gamma pass rate on the validation set did not decrease for 50 epochs. The training was stopped when no improvement was observed at a learning rate of 10^{-6} for 50 epochs.

Model performance for prostate, liver, mamma and head tumor sites are summarized in . Auf die Werte eingehen kurz beschreiben

Comparing the two trained models shows a non significant accuracy decrease for prostate plans and very significant increases for the mixed aswell as the lymphnode test dataset (19.53%, 8.59% for mixed and lymphnode dataset respectively).

Comparing prostate only to mixed trained model is depictedd in fig.

Single segment analysis gives a deeper insight into the actual performance differences of the model. we therefore assessed the gamma passrate for each single segment of all test data (fig ...). Additional information about performance regarding fieldsize can be beneficial

	Prostate	Liver	Mamma	H&N	LN
Number of Patient Plans /1	5	5	5	5	15
Mean Gamma Passrate	97.85	97.59	87.46	90.68	90.71
STD Gamma Passrate /%	2.82	4.56	6.61	6.4	9.6
Median Gamma Passrate	98.59	99.92	86.15	92.74	94.19

Table 3: Summary of gamma passrates for liver, mamma, head and lymphnodes tumor patients
min max hinzufügen

Water slab position /pixel	100		200		300	
Model	Mixed	Prostate	Mixed	Prostate	Mixed	Prostate
Gamma Passrate /%	60.122	56.080	45.539	27.713	48.427	19.246

Table 4: Gamma passrates for prostate only and mixed trained models for different water slab phantom positions inside an air volume. Water slab thickness was 200 pixels.

to predict whether an unseen segment will reach high dose conformity. fig ... shows the analysis for each segment of the test data regarding their fieldsize. additional information about the occurrence of each discretized fieldsize range is shown in the background.

5.4 These 4 / Experiment 4

Both models showed low gamma passrates for all waterslab positions tested. A summary of the accuracy is given in tab. 4. The dose conformity decreases with increasing phantom distance to the accelerator head for the prostate only trained model. The model which was trained on the mixed data set shows better passrates for all slab distances. The transversal view in fig. 11 shows that the prostate model is better at representing the peak at the beginning of the slab than the mixed model for a slab depth of 100 pixels. At higher slab distances the prostate model resembles the qualitative dose distribution quite well, while failing at reaching the correct predictive value. The mixed model can not reach the correct peak height at the beginning but predicts the later curve very well in terms of height and curvature in the transversal view. The coronal and sagittal view both show that the penumbra is resembles very well by both models. At slab depths of 200 and 300 pixels the shoulders of the dose profile drop too fast for the mixed trained model in the coronal view. eingehen auf anstieg bei mixed model im randbereich

6 Discussion

Lorem ipsum dolor sit amet, consetetur sadipscing elitr, sed diam nonumy eirmod tempor invidunt ut labore et dolore magna aliquyam erat, sed diam voluptua. At vero eos et accusam et justo duo dolores et ea rebum. Stet clita kasd gubergren, no sea takimata sanctus est Lorem ipsum dolor sit amet. Lorem ipsum dolor sit amet, consetetur sadipscing elitr, sed diam nonumy eirmod tempor invidunt ut labore et dolore magna aliquyam erat, sed diam voluptua. At vero eos et accusam et justo duo dolores et ea rebum. Stet clita kasd gubergren, no sea takimata sanctus est Lorem ipsum dolor sit amet.

7 Acknowledgement

The authors acknowledge support by the state of Baden-Württemberg through bwHPC and the German Research Foundation (DFG) through grant no INST 39/963-1 FUGG (bwForCluster NEMO).

Literature

- [1] Hans Geinitz, Frank B. Zimmermann, Reinhard Thamm, Andreas Schumertl, Raymond Busch, and Michael Molls: *3D conformal radiation therapy for prostate cancer in elderly patients*. In: Radiotherapy and Oncology 76.1 (July 2005), 27–34. ISSN: 01678140. DOI: 10.1016/j.radonc.2005.06.001. URL: <https://linkinghub.elsevier.com/retrieve/pii/S0167814005002082> (visited on 08/16/2021).
- [2] Tan Dat Nguyen et al.: *The curative role of radiotherapy in adenocarcinoma of the prostate in patients under 55 years of age: A rare cancer network retrospective study*. In: Radiotherapy and Oncology 77.3 (Dec. 2005), 286–289. ISSN: 01678140. DOI: 10.1016/j.radonc.2005.10.015. URL: <https://linkinghub.elsevier.com/retrieve/pii/S0167814005004779> (visited on 08/16/2021).
- [3] Tom Budiharto, Karin Haustermans, and Gyoergy Kovacs: *External Beam Radiotherapy for Prostate Cancer*. In: Journal of Endourology (), 10.
- [4] Joseph Ragaz et al.: *Adjuvant Radiotherapy and Chemotherapy in Node-Positive Premenopausal Women with Breast Cancer*. In: The New England Journal of Medicine (1997), 7.
- [5] Mario De Lena, Roberto Zucali, Giovanni Viganotti, Pinuccia Valagussa, and Gianni Bonadonna: *Combined Chemotherapy-Radiotherapy Approach in Locally Advanced (T3b-T4) Breast Cancer*. In: (), 7.
- [6] Carolyn Taylor et al.: *Estimating the Risks of Breast Cancer Radiotherapy: Evidence From Modern Radiation Doses to the Lungs and Heart and From Previous Randomized Trials*. In: Journal of Clinical Oncology 35.15 (May 20, 2017), 1641–1649. ISSN: 0732-183X. DOI: 10.1200/JCO.2016.72.0722. URL: <https://www.ncbi.nlm.nih.gov/pmc/articles/PMC5548226/> (visited on 08/16/2021).
- [7] N. R. Datta, A. K. Bose, H. K. Kapoor, and S. Gupta: *Head and neck cancers: Results of thermoradiotherapy versus radiotherapy*. In: International Journal of Hyperthermia 6.3 (Jan. 1990), 479–486. ISSN: 0265-6736, 1464-5157. DOI: 10.3109/02656739009140944. URL: <http://www.tandfonline.com/doi/full/10.3109/02656739009140944> (visited on 08/16/2021).
- [8] S.A. Bhide and C.M. Nutting: *Advances in radiotherapy for head and neck cancer*. In: Oral Oncology 46.6 (June 2010), 439–441. ISSN: 13688375. DOI: 10.1016/j.oraloncology.2010.03.005. URL: <https://linkinghub.elsevier.com/retrieve/pii/S1368837510000941> (visited on 08/16/2021).

- [9] Pierre Castadot, John A. Lee, Xavier Geets, and Vincent Grégoire: *Adaptive Radiotherapy of Head and Neck Cancer*. In: *Seminars in Radiation Oncology* 20.2 (Apr. 2010), 84–93. ISSN: 10534296. DOI: 10.1016/j.semradonc.2009.11.002. URL: <https://linkinghub.elsevier.com/retrieve/pii/S1053429609000769> (visited on 08/16/2021).
- [10] Howard E. Morgan and David J. Sher: *Adaptive radiotherapy for head and neck cancer*. In: *Cancers of the Head & Neck* 5.1 (Dec. 2020), 1. ISSN: 2059-7347. DOI: 10.1186/s41199-019-0046-z. URL: <https://cancersheadneck.biomedcentral.com/articles/10.1186/s41199-019-0046-z> (visited on 08/16/2021).
- [11] Morten Høyer, Anand Swaminath, Sean Bydder, Michael Lock, Alejandra Méndez Romero, Brian Kavanagh, Karyn A. Goodman, Paul Okunieff, and Laura A. Dawson: *Radiotherapy for Liver Metastases: A Review of Evidence*. In: *International Journal of Radiation Oncology*Biology*Physics* 82.3 (Mar. 1, 2012), 1047–1057. ISSN: 0360-3016. DOI: 10.1016/j.ijrobp.2011.07.020. URL: <https://www.sciencedirect.com/science/article/pii/S0360301611030902> (visited on 08/16/2021).
- [12] Jörn Wulf, Ulrich Hädinger, Ulrich Oppitz, Wibke Thiele, Rea Ness-Dourdoumas, and Michael Flentje: *Stereotactic Radiotherapy of Targets in the Lung and Liver*: in: *Strahlentherapie und Onkologie* 177.12 (Dec. 2001), 645–655. ISSN: 0179-7158. DOI: 10.1007/PL00002379. URL: <http://link.springer.com/10.1007/PL00002379> (visited on 08/16/2021).
- [13] Joern Wulf, Matthias Guckenberger, Ulrich Haedinger, Ulrich Oppitz, Gerd Mueller, Kurt Baier, and Michael Flentje: *Stereotactic radiotherapy of primary liver cancer and hepatic metastases*. In: *Acta Oncologica* 45.7 (Jan. 2006), 838–847. ISSN: 0284-186X, 1651-226X. DOI: 10.1080/02841860600904821. URL: <http://www.tandfonline.com/doi/full/10.1080/02841860600904821> (visited on 08/16/2021).
- [14] Florian Sterzing, Thomas B. Brunner, Iris Ernst, Wolfgang W. Baus, Burkhard Greve, Klaus Herfarth, and Matthias Guckenberger: *Stereotactic body radiotherapy for liver tumors: Principles and practical guidelines of the DEGRO Working Group on Stereotactic Radiotherapy*. In: *Strahlentherapie und Onkologie* 190.10 (Oct. 2014), 872–881. ISSN: 0179-7158, 1439-099X. DOI: 10.1007/s00066-014-0714-1. URL: <http://link.springer.com/10.1007/s00066-014-0714-1> (visited on 08/16/2021).
- [15] Jacob S Witt, Stephen A Rosenberg, and Michael F Bassetti: *MRI-guided adaptive radiotherapy for liver tumours: visualising the future*. In: *The Lancet Oncology* 21.2 (Feb. 1, 2020), e74–e82. ISSN: 1470-2045. DOI: 10.1016/S1470-2045(20)

- 30034–6. URL: <https://www.sciencedirect.com/science/article/pii/S1470204520300346> (visited on 08/16/2021).
- [16] Breast Cancer Expert Panel of the German Society of Radiation Oncology (DEGRO) et al.: *DEGRO practical guidelines for radiotherapy of breast cancer IV: Radiotherapy following mastectomy for invasive breast cancer*. In: *Strahlentherapie und Onkologie* 190.8 (Aug. 2014), 705–714. ISSN: 0179-7158, 1439-099X. DOI: 10.1007/s00066-014-0687-0. URL: <http://link.springer.com/10.1007/s00066-014-0687-0> (visited on 08/16/2021).
- [17] Haruo Matsushita, Keiichi Jingu, Rei Umezawa, Takaya Yamamoto, Yojiro Ishikawa, Noriyoshi Takahashi, Yu Katagiri, and Noriyuki Kadoya: *Stereotactic Radiotherapy for Oligometastases in Lymph Nodes—A Review*. In: *Technology in Cancer Research & Treatment* 17 (Jan. 2018), 153303381880359. ISSN: 1533-0346, 1533-0338. DOI: 10.1177/1533033818803597. URL: <http://journals.sagepub.com/doi/10.1177/1533033818803597> (visited on 08/16/2021).
- [18] John L. Mikell et al.: *Postoperative Radiotherapy is Associated with Better Survival in Non-Small Cell Lung Cancer with Involved N2 Lymph Nodes: Results of an Analysis of the National Cancer Data Base*. In: *Journal of Thoracic Oncology* 10.3 (Mar. 2015), 462–471. ISSN: 15560864. DOI: 10.1097/JTO.0000000000000411. URL: <https://linkinghub.elsevier.com/retrieve/pii/S1556086415316543> (visited on 08/16/2021).
- [19] Dan Lundstedt, Magnus Gustafsson, Gunnar Steineck, David Alsadius, Agnetha Sundberg, Ulrica Wilderäng, Erik Holmberg, Karl-Axel Johansson, and Per Karlsson: *Long-term symptoms after radiotherapy of supraclavicular lymph nodes in breast cancer patients*. In: *Radiotherapy and Oncology* 103.2 (May 2012), 155–160. ISSN: 01678140. DOI: 10.1016/j.radonc.2011.12.017. URL: <https://linkinghub.elsevier.com/retrieve/pii/S0167814011007572> (visited on 08/16/2021).
- [20] Barbara Alicja Jereczek-Fossa, Sara Ronchi, and Roberto Orecchia: *Is Stereotactic Body Radiotherapy (SBRT) in lymph node oligometastatic patients feasible and effective?* In: *Reports of Practical Oncology and Radiotherapy* 20.6 (2015), 472–483. ISSN: 1507-1367. DOI: 10.1016/j.rpor.2014.10.004. URL: <https://www.ncbi.nlm.nih.gov/pmc/articles/PMC4661354/> (visited on 08/16/2021).
- [21] Samaneh Kazemifar, Anjali Balagopal, Dan Nguyen, Sarah McGuire, Raquibul Hannan, Steve Jiang, and Amir Owringi: *Segmentation of the prostate and organs at risk in male pelvic CT images using deep learning*. In: *Biomedical Physics & Engineering Express* 4.5 (July 23, 2018), 055003. ISSN: 2057-1976. DOI: 10.1088/2057-

- 1976/aad100. URL: <https://iopscience.iop.org/article/10.1088/2057-1976/aad100> (visited on 08/23/2021).
- [22] Shujun Liang, Fan Tang, Xia Huang, Kaifan Yang, Tao Zhong, Runyue Hu, Shangqing Liu, Xinrui Yuan, and Yu Zhang: *Deep-learning-based detection and segmentation of organs at risk in nasopharyngeal carcinoma computed tomographic images for radiotherapy planning*. In: *European Radiology* 29.4 (Apr. 2019), 1961–1967. ISSN: 0938-7994, 1432-1084. DOI: 10.1007/s00330-018-5748-9. URL: <http://link.springer.com/10.1007/s00330-018-5748-9> (visited on 08/23/2021).
- [23] Dinggang Shen, Tianming Liu, Terry M. Peters, Lawrence H. Staib, Caroline Es-sert, Sean Zhou, Pew-Thian Yap, and Ali Khan, eds.: *Medical Image Computing and Computer Assisted Intervention – MICCAI 2019: 22nd International Conference, Shenzhen, China, October 13–17, 2019, Proceedings, Part II*. Vol. 11765. Lecture Notes in Computer Science. Cham: Springer International Publishing, 2019. ISBN: 978-3-030-32244-1 978-3-030-32245-8. DOI: 10.1007/978-3-030-32245-8. URL: <https://link.springer.com/10.1007/978-3-030-32245-8> (visited on 08/23/2021).
- [24] Jiawei Fan, Jiazhou Wang, Zhi Chen, Chaosu Hu, Zhen Zhang, and Weigang Hu: *Automatic treatment planning based on three-dimensional dose distribution predicted from deep learning technique*. In: *Medical Physics* 46.1 (Jan. 2019), 370–381. ISSN: 00942405. DOI: 10.1002/mp.13271. URL: <http://doi.wiley.com/10.1002/mp.13271> (visited on 03/16/2021).
- [25] Zhiqiang Liu, Jiawei Fan, Minghui Li, Hui Yan, Zhihui Hu, Peng Huang, Yuan Tian, Junjie Miao, and Jianrong Dai: *A deep learning method for prediction of three-dimensional dose distribution of helical tomotherapy*. In: *Medical Physics* 46.5 (May 2019), 1972–1983. ISSN: 0094-2405, 2473-4209. DOI: 10.1002/mp.13490. URL: <https://onlinelibrary.wiley.com/doi/abs/10.1002/mp.13490> (visited on 03/16/2021).
- [26] C. Kontaxis, G. H. Bol, J. J. W. Lagendijk, and B. W. Raaymakers: *DeepDose: Towards a fast dose calculation engine for radiation therapy using deep learning*. In: *Physics in Medicine & Biology* 65.7 (Apr. 2020). Publisher: IOP Publishing, 075013. ISSN: 0031-9155. DOI: 10.1088/1361-6560/ab7630. URL: <https://doi.org/10.1088/1361-6560/ab7630> (visited on 08/23/2021).
- [27] Ti Bai, Biling Wang, Dan Nguyen, and Steve Jiang: *Deep dose plugin: towards real-time Monte Carlo dose calculation through a deep learning-based denoising algorithm*. In: *Machine Learning: Science and Technology* 2.2 (June 1, 2021), 025033.

- ISSN: 2632-2153. DOI: 10.1088/2632-2153/abdbfe. URL: <https://iopscience.iop.org/article/10.1088/2632-2153/abdbfe> (visited on 08/23/2021).
- [28] Xiao Han: *MR-based synthetic CT generation using a deep convolutional neural network method*. In: Medical Physics 44.4 (2017). _eprint: <https://aapm.onlinelibrary.wiley.com/doi/abs/10.1002/mp.12155>. ISSN: 2473-4209. DOI: 10.1002/mp.12155. URL: <https://aapm.onlinelibrary.wiley.com/doi/abs/10.1002/mp.12155> (visited on 08/23/2021).
- [29] Jelmer M. Wolterink, Anna M. Dinkla, Mark H. F. Savenije, Peter R. Seevinck, Cornelis A. T. van den Berg, and Ivana Išgum: *Deep MR to CT Synthesis Using Unpaired Data*. In: *Simulation and Synthesis in Medical Imaging*. Ed. by Sotirios A. Tsaftaris, Ali Gooya, Alejandro F. Frangi, and Jerry L. Prince. Lecture Notes in Computer Science. Cham: Springer International Publishing, 2017, 14–23. ISBN: 978-3-319-68127-6. DOI: 10.1007/978-3-319-68127-6_2.
- [30] Anna M. Dinkla, Jelmer M. Wolterink, Matteo Maspero, Mark H.F. Savenije, Joost J.C. Verhoeff, Enrica Seravalli, Ivana Išgum, Peter R. Seevinck, and Cornelis A.T. van den Berg: *MR-Only Brain Radiation Therapy: Dosimetric Evaluation of Synthetic CTs Generated by a Dilated Convolutional Neural Network*. In: International Journal of Radiation Oncology*Biophysics 102.4 (Nov. 2018), 801–812. ISSN: 03603016. DOI: 10.1016/j.ijrobp.2018.05.058. URL: <https://linkinghub.elsevier.com/retrieve/pii/S0360301618309106> (visited on 08/23/2021).
- [31] Olaf Ronneberger, Philipp Fischer, and Thomas Brox: *U-Net: Convolutional Networks for Biomedical Image Segmentation*. In: arXiv:1505.04597 [cs] (May 18, 2015). arXiv: 1505.04597. URL: <http://arxiv.org/abs/1505.04597> (visited on 11/03/2021).
- [32] Fernando Pérez-García, Rachel Sparks, and Sébastien Ourselin: *TorchIO: A Python library for efficient loading, preprocessing, augmentation and patch-based sampling of medical images in deep learning*. In: Computer Methods and Programs in Biomedicine 208 (Sept. 2021), 106236. ISSN: 01692607. DOI: 10.1016/j.cmpb.2021.106236. URL: <https://linkinghub.elsevier.com/retrieve/pii/S0169260721003102> (visited on 11/03/2021).
- [33] *nrc-cnrc/EGSnrc*. original-date: 2012-11-28T19:26:41Z. Aug. 7, 2021. URL: <https://github.com/nrc-cnrc/EGSnrc> (visited on 08/17/2021).
- [34] M. Friedel, M. Nachbar, D. Mönnich, O. Dohm, and D. Thorwarth: *Development and validation of a 1.5 T MR-Linac full accelerator head and cryostat model for Monte Carlo dose simulations*. In: Medical Physics 46.11 (Nov. 2019), 5304–5313. ISSN:

0094-2405, 2473-4209. DOI: 10.1002/mp.13829. URL: <https://onlinelibrary.wiley.com/doi/abs/10.1002/mp.13829> (visited on 03/16/2021).

- [35] Daniel A. Low, William B. Harms, Sasa Mutic, and James A. Purdy: *A technique for the quantitative evaluation of dose distributions*. In: Medical Physics 25.5 (May 1998), 656–661. ISSN: 00942405. DOI: 10.1118/1.598248. URL: <http://doi.wiley.com/10.1118/1.598248> (visited on 03/16/2021).

Apendix

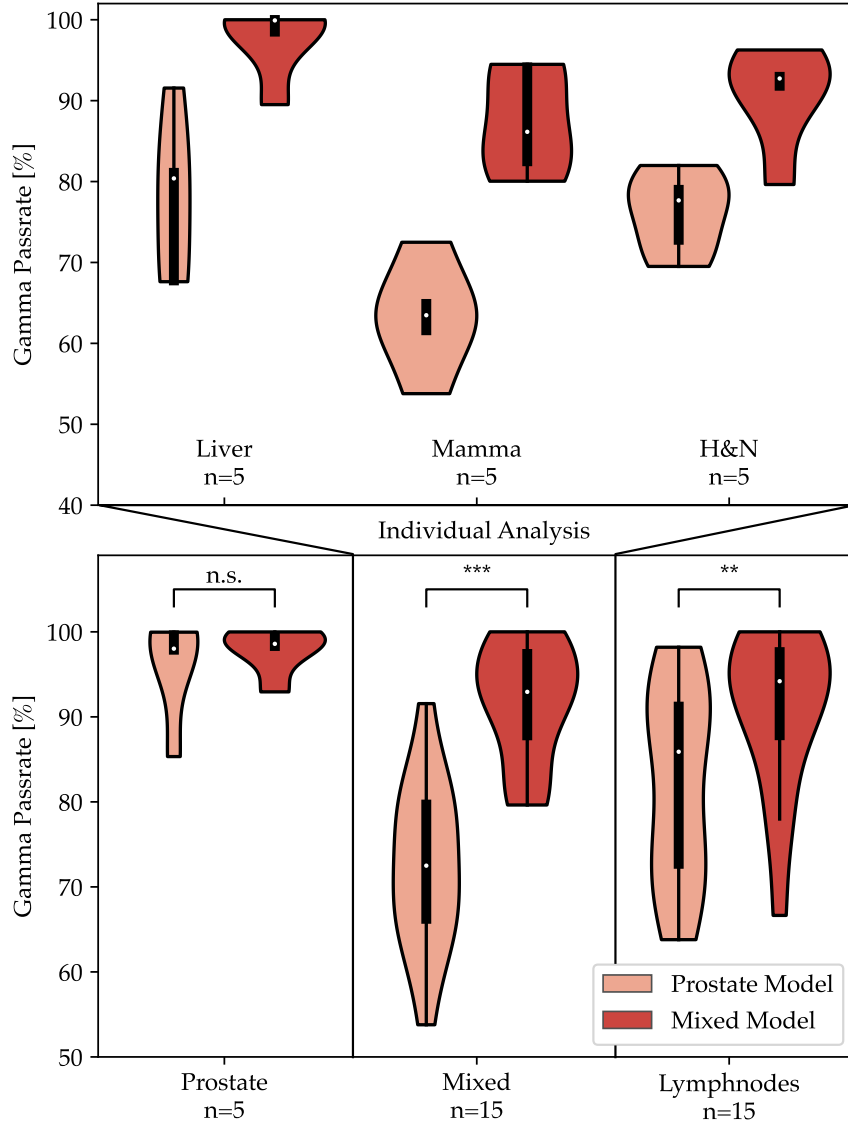


Figure 8: Prediction accuracy comparison between prostate only and mixed trained models. Passrates for liver, mamma and H&N are combined into one group of ‘mixed’ data. Significance level using a wilcoxon signed-ranked test are shown above the compared datasets. zusätzlich plot für einzelne entities also leber, mamma, h&N einzeln, sternchen erklären oder direkt obendrüber schreiben, feste convention finden wie ich die beiden Model nennen will

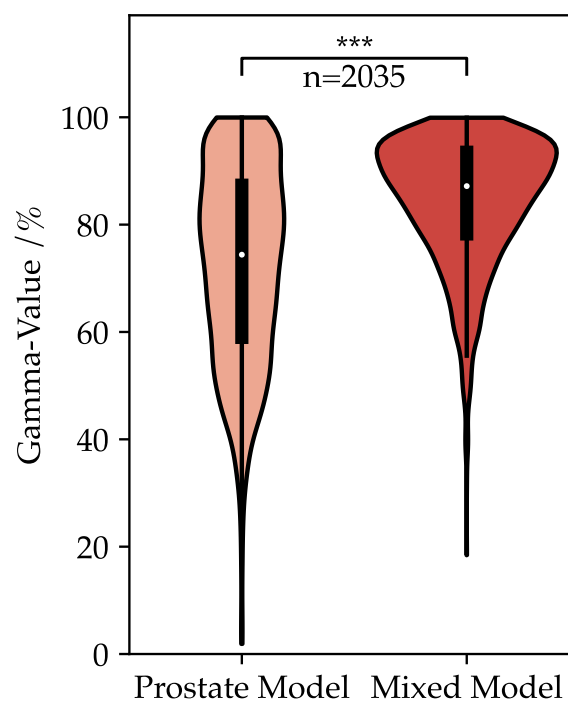


Figure 9: Prediction accuracy for all segments of the test data.

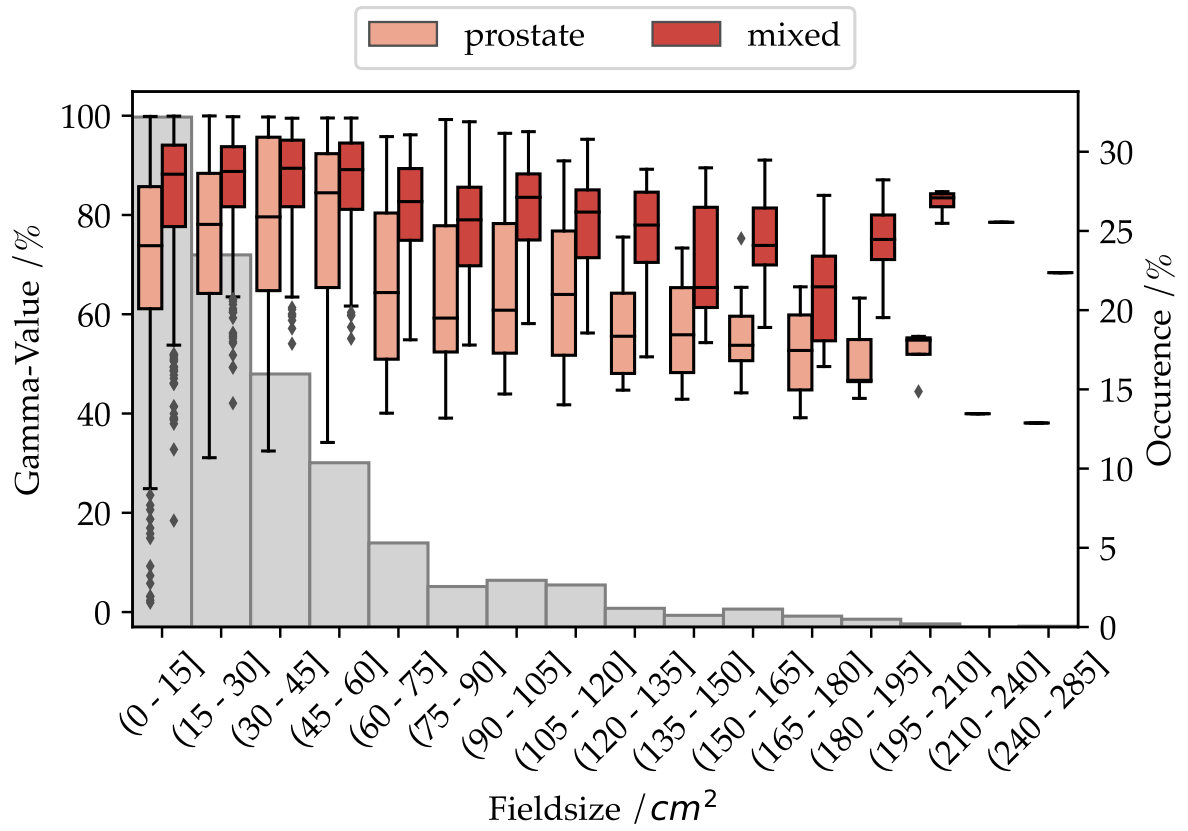


Figure 10: Prediction accuracy of each segment with respect to field size for prostate only and mixed trained model.

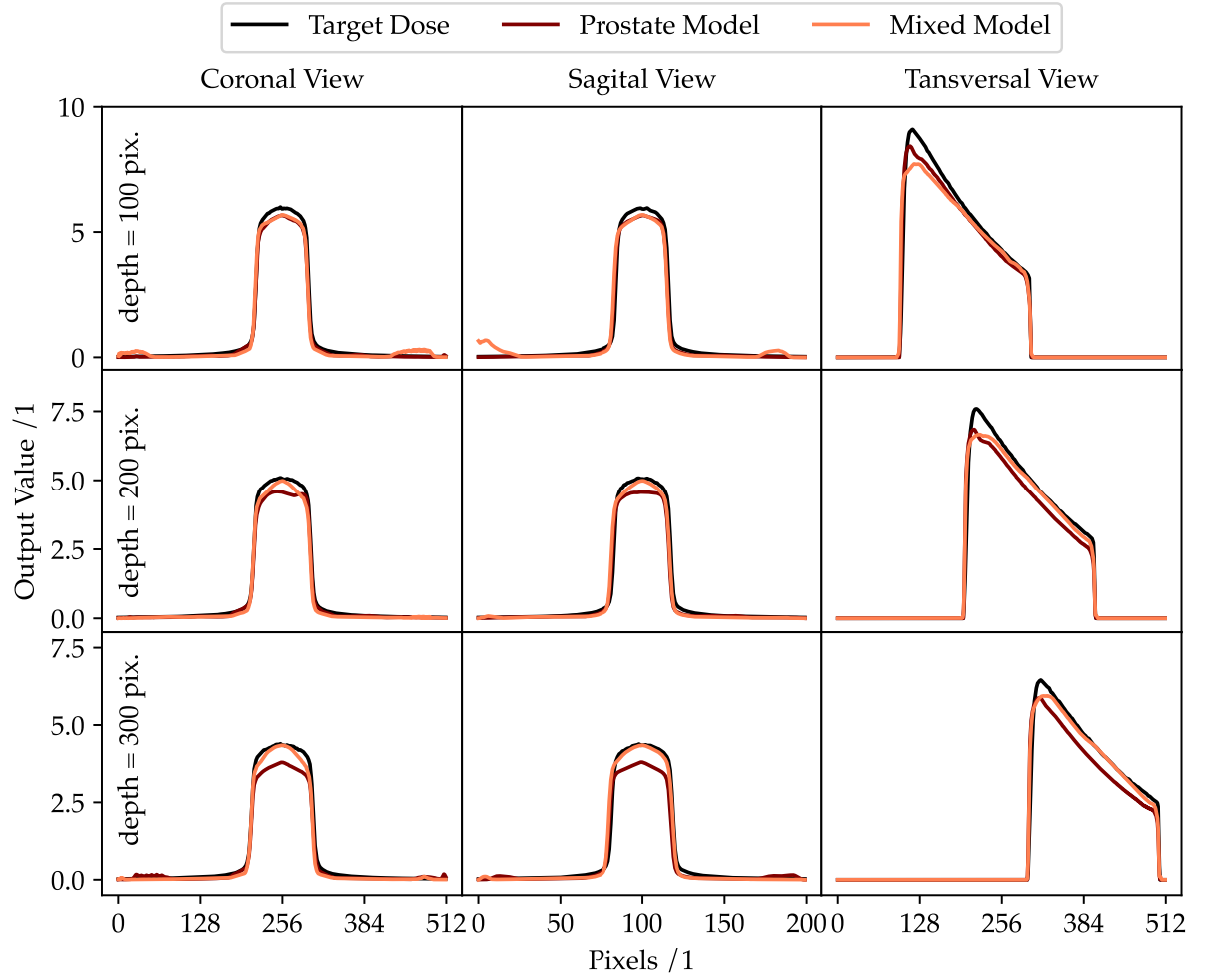


Figure 11: Coronal, sagittal and transversal view of the dose distributions for 100, 200 and 300 px depth in the phantom volume